

SCIENTIFIC REPORTS

OPEN

Mechanical diagnosis of human erythrocytes by ultra-high speed manipulation unraveled critical time window for global cytoskeletal remodeling

Hiroaki Ito^{1,2}, Ryo Murakami¹, Shinya Sakuma³, Chia-Hung Dylan Tsai¹, Thomas Gutschmann⁴, Klaus Brandenburg⁴, Johannes M. B. Pöschl⁵, Fumihito Arai³, Makoto Kaneko¹ & Motomu Tanaka^{6,7}

Received: 25 October 2016
Accepted: 19 January 2017
Published: 24 February 2017

Large deformability of erythrocytes in microvasculature is a prerequisite to realize smooth circulation. We develop a novel tool for the three-step “Catch-Load-Launch” manipulation of a human erythrocyte based on an ultra-high speed position control by a microfluidic “robotic pump”. Quantification of the erythrocyte shape recovery as a function of loading time uncovered the critical time window for the transition between fast and slow recoveries. The comparison with erythrocytes under depletion of adenosine triphosphate revealed that the cytoskeletal remodeling over a whole cell occurs in 3 orders of magnitude longer timescale than the local dissociation-reassociation of a single spectrin node. Finally, we modeled septic conditions by incubating erythrocytes with endotoxin, and found that the exposure to endotoxin results in a significant delay in the characteristic transition time for cytoskeletal remodeling. The high speed manipulation of erythrocytes with a robotic pump technique allows for high throughput mechanical diagnosis of blood-related diseases.

Erythrocytes are known for their significant tolerance against large shape deformation in microvasculature, many of which are much narrower compared to their average diameter. Since ample evidence suggested a tight correlation between the deformability and plasticity in cell deformation and diseases, the viscoelastic parameters of human erythrocytes have been evaluated by various experimental techniques, e.g., micropipette aspiration^{1–4}, optical tweezers^{5–9}, and flicker spectroscopy^{10–13}. Although these techniques can provide detailed viscoelastic parameters of erythrocytes, they suffer from low throughput due to manual handling of erythrocytes under microscopy. Cone-plate rheometer^{14,15} and microfluidic on-chip platforms^{16–18} have also been used frequently as high throughput evaluation techniques, but the output of these techniques is mainly the “deformability”. This coincides with an aspect ratio of the deformed cell, which is a less informative index merely reflecting the shear modulus. Optical stretcher^{19,20} and deformability cytometry^{21,22} are recent attempts to overcome the trade-off between the throughput and information content^{23,24} with aid of the mathematical calculation of small deformations in these systems^{25,26}. However, the evaluation of small deformation is not directly relevant to quantify the mechanical response of erythrocytes to the large degree of deformation, which they physiologically experience in microvasculatures. Thus, a high throughput diagnostic tool assessing the mechanical response of erythrocytes under large deformation is strongly demanded.

¹Department of Mechanical Engineering, Osaka University, 565-0871 Suita, Japan. ²Department of Physics, Kyoto University, 606-8502 Kyoto, Japan. ³Department of Micro-Nano Systems Engineering, Nagoya University, 464-8603 Nagoya, Japan. ⁴Research Center Borstel, D23845 Borstel, Germany. ⁵Department of Pediatrics, Clinic of Neonatology, University of Heidelberg, D69120 Heidelberg, Germany. ⁶Institute of Physical Chemistry, University of Heidelberg, D69120 Heidelberg, Germany. ⁷Institute for Integrated Cell-Material Sciences (WPI iCeMS), Kyoto University, 606-8501 Kyoto, Japan. Correspondence and requests for materials should be addressed to M.K. (email: mk@mech.eng.osaka-u.ac.jp) or M.T. (email: tanaka@uni-heidelberg.de)

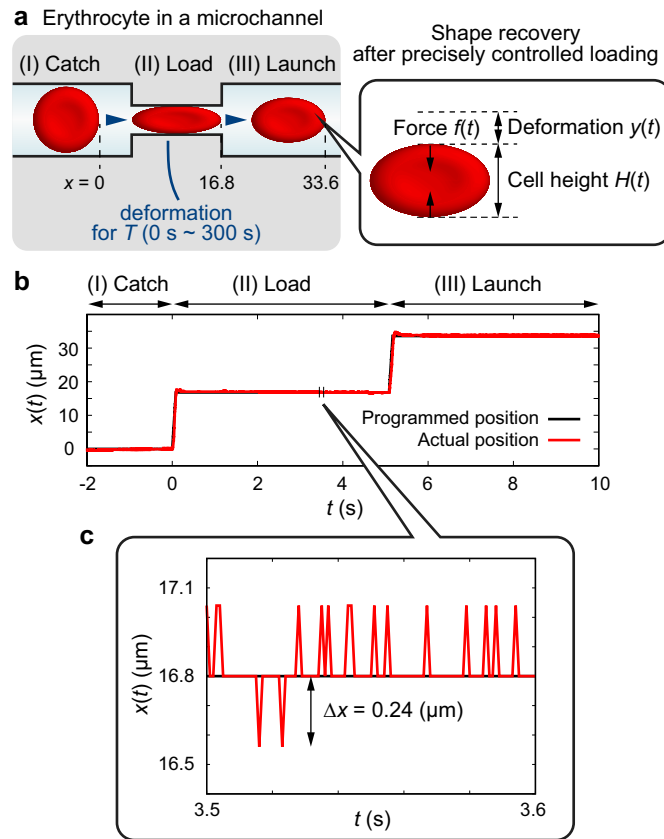


Figure 1. On-chip “Catch-Load-Launch” manipulation of an erythrocyte with the aid of a robotic pump system. (a) Schematic diagram of the manipulation. An erythrocyte is first (I) arrested at the entrance (Catch), (II) kept in the narrow path for a distinct time T (Load), and (III) released from the narrow path (Launch). (b) An example of the actual cell position $x(t)$ (red) and the programmed position (black). (c) Magnified plot of time window of 100 ms.

When erythrocytes undergo a large deformation, global cytoskeletal remodeling plays an important role in the shape adaptation. There have been experimental and theoretical studies demonstrating that the remodeling of spectrin cytoskeleton depends on the concentration of adenosine triphosphate (ATP)²⁰ and shearing force^{27,28}. Recent shape fluctuation analyses confirmed the discrepancy in the fluctuation spectrum between the intact and ATP-depleted states^{8,29} and the violation of fluctuation-dissipation theorem^{9,30}. The characteristic time window, about 100 ms, can be attributed to the dissociation-reassociation process of a single node of the triangular spectrin lattice. Although biochemical factors, such as ATP concentration and protein phosphorylation, regulate such a local dynamics and active small fluctuation, the global remodeling in response to the large deformation requires much longer timescale, which has never been assessed in a systematic manner.

In the present work, we developed a novel high throughput assay to quantify the mechanical response of erythrocytes after spatial constriction mimicking microvasculature environments. One of the technical challenges is the precise cell manipulation inside a narrow channel, because the system should be highly sensitive to sustain a delicate balance between pressure and flow velocity. Here, we utilized a “robotic-pump”^{31,32} to manipulate an erythrocyte inside a narrow microfluidic path. The erythrocyte was precisely localized in the microchannel by the combination of an ultra-high speed pressure control unit and a real time visual feedback. This enables one to “catch” an erythrocyte in front of the constriction, “load” it inside for a desired time, and quickly “launch” it from the constriction to monitor the shape recovery over time. Using such a “Catch-Load-Launch” manipulation platform, we compared the shape recovery of human erythrocytes in the presence and absence of ATP. The systematic variation of loading time enables us to uncover the characteristic time window for the global spectrin remodeling. Moreover, as a preliminary model of sepsis, we monitored the mechanical response of erythrocytes in the presence of endotoxin (lipopolysaccharide, LPS).

Results

“Catch-Load-Launch” manipulation. Figure 1a schematically represents the “Catch-Load-Launch” manipulation of an erythrocyte on a microfluidic chip. The microfluidic channel with $10\mu\text{m} \times 3.5\mu\text{m}$ rectangular cross section has a narrow path in the middle (cross section: $3\mu\text{m} \times 3.5\mu\text{m}$) that mimics the narrowest spatial constriction in microvasculatures of human spleen³³ to investigate the large deformation of erythrocytes. In the resting state, a biconcave erythrocyte (discocyte) with typical diameter of $8\mu\text{m}$ and height of $2\mu\text{m}$ is lying in a “thin” microchannel with the height of $3.5\mu\text{m}$. Thus, the projected images of erythrocytes are circular. First, an

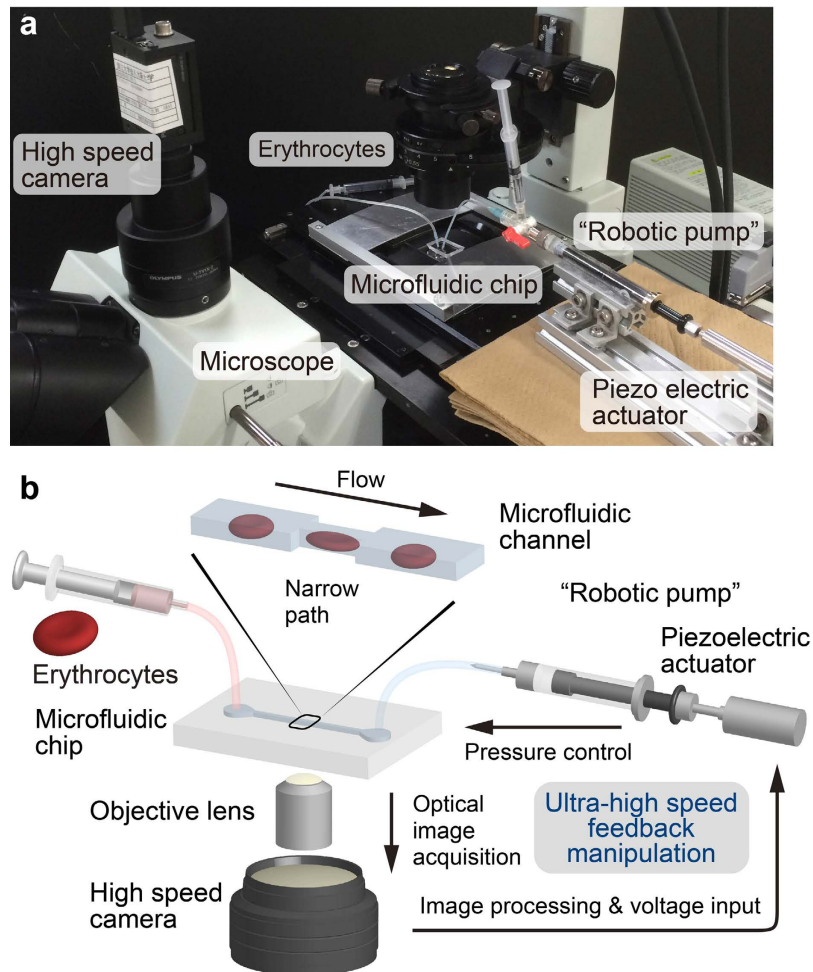


Figure 2. Ultra-high speed feedback system to control the cell position inside a microchannel. (a) Experimental setup and (b) its detailed schematic diagram. Ultra-high speed (1000 Hz) visual feedback system composed of a high-speed camera and a piezoelectric actuator connected to a syringe provides the pressure control at the channel outlet, enabling the precise cell manipulation ($\Delta x = \pm 0.24 \mu\text{m}$) inside the narrow path (cross section: $3 \mu\text{m} \times 3.5 \mu\text{m}$).

erythrocyte is caught in front of the narrow path and kept for 2 s to record the original shape (Catch). Second, the cell is transferred into the narrow path and stressed by a constriction force $f(t)$ for a programmed time $T = 0 \text{ s}$, 5 s, 15 s, 30 s, 45 s, 60 s, 120 s, 180 s, and 300 s (Load). Finally, the cell is ejected from the narrow path (Launch). Changes in cell deformation $y(t)$ and cell height $H(t)$ are recorded as a function of time. The channel length for the launch phase is designed to be $10 \mu\text{m}$, which is practically the shortest length for erythrocytes (diameter $\approx 8 \mu\text{m}$). It should be noted that the channel is explicitly used for the spatial constriction of the cell position and thus the channel length does not affect the dynamics of shape recovery. Figure 1b exemplifies the cell position $x(t)$ recorded in the Catch-Load-Launch manipulation. The actual position (red) precisely follows the programmed position (black) in a step-like way. The programmed velocity dx/dt in the step-like motion is set to $200 \mu\text{m/s}$ for sufficiently fast and stable manipulation. The spatial resolution of the manipulation is $\Delta x = \pm 0.24 \mu\text{m}$, which corresponds to a minimum pixel size in the present experiment (Fig. 1c).

Precise, real time control of the cell position $x(t)$ is achieved with aid of a “robotic pump” system, enabling the ultra-high speed feedback control of the pressure at the outlet of the microchannel (Fig. 2a, see also Methods for further information). The feedback system is composed of a microscope equipped with a high speed camera and a piezoelectric actuator connected to a syringe. As schematically illustrated in Fig. 2b, the optical images acquired by a high speed camera are processed by a computer, and the detected cell position is converted to voltage information by proportional-integral-derivative (PID) algorithm. The calculated voltage value is then entered into a piezoelectric actuator and further converted to the pressure of a connected syringe, resulting in the manipulation of the cell position $x(t)$ within the pixel resolution ($\Delta x = \pm 0.24 \mu\text{m}$). We set the frequency of image acquisition at 1000 Hz to capture the cell, because the typical residence time of a flowing erythrocyte in the camera view is a few ms. This enables the catch, load, and launch of the cell at an ultra-high spatiotemporal resolution under optical microscopy, which cannot be realized otherwise. The capability not only to manipulate but also to record the image of the target cell every 1 ms is advantageous over other fast spectroscopy^{8,29} because one can clearly distinguish the fast elastic response, viscoelastic relaxation, and plastic deformation after the launch.

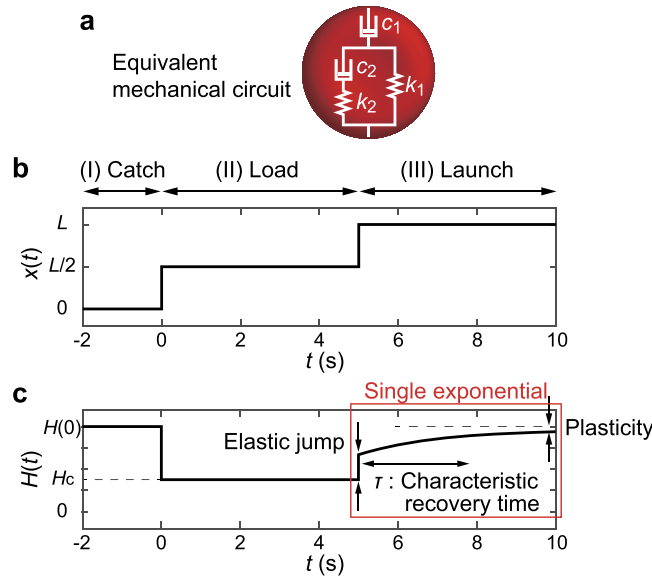


Figure 3. Typical analytical representation of standard linear elastic (SLE) model in (I) Catch, (II) Load, and (III) Launch phases. (a) Equivalent mechanical circuit that consists of two springs (spring constants: k_1 , k_2) and two dampers (viscous coefficients: c_1 , c_2). (b) Mathematical representation of the cell position $x(t)$ (equation (3)). (c) Changes in cell height $H(t)$ (equation (4)), calculated from equations (1) and (3). In the linear viscoelastic regime, the shape recovery in the launching phase (III) (red square in c) is represented by a single exponential function. For plotting, parameters are set to $k_1 = 1 \text{ N}/\mu\text{m}$, $k_2 = 1 \text{ N}/\mu\text{m}$, $c_1 = 100 \text{ N}\cdot\text{s}/\mu\text{m}$, $c_2 = 1 \text{ N}\cdot\text{s}/\mu\text{m}$, $H(0) = 8 \mu\text{m}$, and $T = 5 \text{ s}$ despite the arbitrariness of force unit.

Analysis of erythrocyte deformation. After the large deformation inside the narrow path, the launched erythrocyte exhibits a dynamic shape recovery. Although the actual deformation and the shape recovery include both restoration from stretching and folding, we assume a coupled linear viscoelastic elements for mathematical description of the observed cell shape. In fact, the temporal change in cell height obtained from the experimental data could be well explained by a single exponential curve (Fig. 3). Figure 3a shows a typical analytical solution of a standard linear elastic (SLE) model composed of two linear springs (spring constants: k_1 and k_2) and two linear dampers (viscous coefficients: c_1 and c_2). We used the SLE model as the minimal model, since the simpler models such as Voigt model cannot reproduce all the mechanical responses of biological cells, force relaxation, creep, and plastic flow³⁴. The constitutive equation of the SLE model is

$$\ddot{y} + \frac{1}{\tau}\dot{y} = \frac{1}{k_1 + k_2}\ddot{f} + \left(\frac{1}{k_1\tau} + \frac{1}{c_2}\right)\dot{f} + \frac{1}{c_1\tau}f, \quad (1)$$

where the characteristic time constant of the shape recovery is represented by

$$\tau \equiv \frac{c_2(k_1 + k_2)}{k_1k_2}. \quad (2)$$

Note that the characteristic recovery time τ is independent of the loading time T , and therefore an intrinsic material constant. The Catch-Load-Launch manipulation of the cell position $x(t)$ can be mathematically approximated as an ideal step function (Fig. 3b, $T = 5 \text{ s}$ as an example):

$$x(t) = \begin{cases} 0, & (t < 0) \\ \frac{L}{2}, & (0 \leq t < T) \\ L, & (T \leq t), \end{cases} \quad (3)$$

where $L = 33.6 \mu\text{m}$ is the total distance that a cell moves from “catch” to “launch”. Figure 3c represents the calculated cell height $H(t)$ ($= H(0) - y(t)$) during the manipulation. $H(0)$ is the initial height of the target cell measured prior to the loading. $H_c = 3 \mu\text{m}$ is the constriction width of the narrow path, which corresponds to the cell height in the loading phase. The analytical solution $H(t)$ of equation (1) after the launch ($t \geq T$) takes a single exponential function:

$$H(t) = H(0) - \left(A_1 + A_2 e^{-\frac{t-T}{\tau}}\right), \quad (4)$$

where A_1 and A_2 are constant (see Methods for more details). Thus, $H(t)$ is characterized by three information: Elastic jump $H(0) - (A_1 + A_2) - H_c$, plasticity A_1 , and characteristic recovery time τ (red square in Fig. 3c).

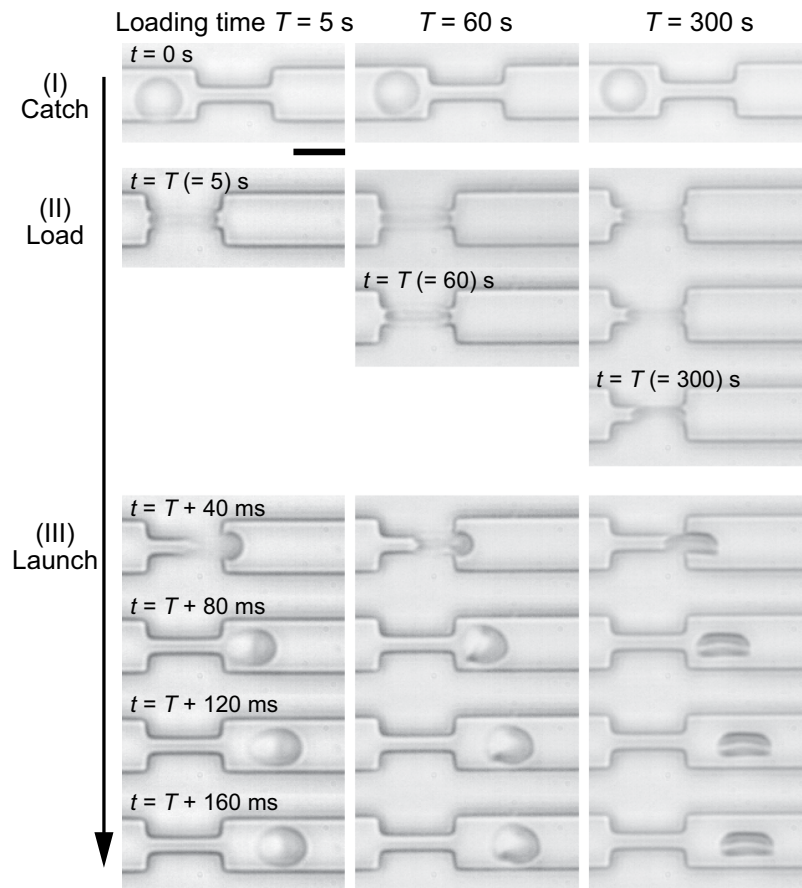


Figure 4. Snapshot images of erythrocytes in “Catch-Load-Launch” process in the cases of loading times $T = 5$ s (left), 60 s (middle), and 300 s (right). After the launch from the narrow path, the cell undergoes shape recovery. The shape recovery becomes drastically slower as the loading time T becomes of the order of 100 s. Scale bar is 10 μm .

Shape recovery after launching. Figure 4 shows typical snapshot images recorded in the three-step manipulation for various loading times: $T = 5$ s (left), 60 s (middle), and 300 s (right). The data from other conditions ($T = 0$ s, 15 s, and 180 s) are presented in Supplementary Fig. S1. In the catching phase (I), the shape of an erythrocyte projected onto a two-dimensional image is almost circular, corresponding to a normal discocyte. In the loading phase (II), the target cell is largely deformed in a constriction, kept for a specified loading time T . The end of the loading at $t = T$ is the initial condition for shape recovery after the launch. Finally, in the launching phase (III), shape recovery of the ejected cell is monitored as a function of time. When the cell is loaded only for $T = 5$ s, the shape recovery occurs within hundreds of ms. On the other hand, after being kept in the narrow path for $T = 300$ s, the cell no longer recovers its original shape in hundreds of ms. It should be noted that some erythrocytes take triangular or parachute-like shape (e.g., $t = 60$ s + 80 ms in Fig. 4) due to the hydrodynamic or mechanical frictions during the rapid launching^{35–37}.

Circular symbols in Fig. 5a represent mean temporal changes in the normalized cell height $H(t)/H(0)$ over 60 s for intact erythrocytes that were loaded in the narrow path for $T = 5$ s, 60 s, 180 s, and 300 s. The data for $T = 0$ s and 15 s are presented in Supplementary Fig. S2. As schematically shown in the inset of Fig. 5a, $H(t)$ was determined along the minor axis of the cell at every moment with the aid of real-space imaging. A small but distinct overshoot observed at $t = T + 50$ –80 ms can be attributed to the geometrical artifact from the cell taking a triangular shape, which is more pronounced for shorter loading time T due to significant elastic response. At $t > 80$ –100 ms, the cell shape restored front-rear symmetry and exhibited the viscoelastic shape recovery from ellipsoidal to circular, which was subjected to the SLE analysis. Figure 5b shows the representative snapshot images of erythrocytes at $t = 150$ ms after the launch, which corresponds to the various loading time conditions shown in Fig. 5a. We found that the characteristic recovery time increases from $\tau \sim 0.1$ s to 10 s in accordance with the increase in the loading time T from 5 s to 300 s. A distinct dependence of τ on T is in clear contrast to the common viscoelastic materials, whose recovery dynamics is independent of the stress duration. It should also be noted that the shape recovery becomes drastically slower ($\tau \sim 10$ s) when the loading time T becomes longer than the critical loading time $T_c \sim 180$ s.

Influence of ATP-depletion. The significant deformation and shape recovery through “Catch-Load-Launch” manipulation naturally suggest that such a process is accompanied with the global

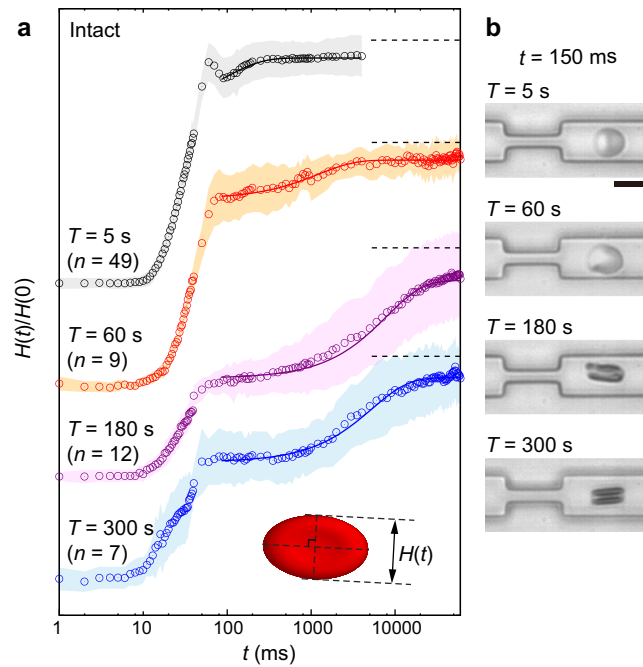


Figure 5. Change in cell height $H(t)$ over time, recorded for intact erythrocytes for the different loading times T : 5 s, 60 s, 180 s, and 300 s. **(a)** Normalized cell height $H(t)/H(0)$. The standard deviations and the fitting curves are represented by shaded areas and solid lines, respectively. Dotted lines represent $H(t)/H(0) = 1$ for each T . Each number of samples n is shown above the graph. Inset shows the definition of $H(t)$, which is measured along minor axis of the shape. **(b)** Representative snapshot image for each T . Scale bar is $10\mu\text{m}$.

remodeling of cytoskeletons. As the dynamic remodeling of spectrin cytoskeletons strongly depends on ATP concentrations, we measured the shape recovery of erythrocytes under ATP-depletion (Fig. 6a and b) and compared them with intact erythrocytes (Fig. 6c). Figure 6a shows mean temporal changes in the normalized cell height $H(t)/H(0)$ over 60 s for ATP-depleted erythrocytes that were loaded in the narrow path for $T = 5$ s, 60 s, 180 s, and 300 s. The data for $T = 0$ s and 15 s are presented in Supplementary Fig. S2. In cases of $T = 5$ s and 60 s, the recovery of the normalized cell height $H(t)/H(0)$ under ATP-depletion was slightly faster than that of intact erythrocytes, as the difference $H(t)/H(0)|_{\text{ATP-depleted}} - H(t)/H(0)|_{\text{intact}}$ becomes positive (Fig. 6c). This result suggests that the elastic feature becomes relatively significant compared to the viscous feature in ATP-depleted erythrocytes. Moreover, since ATP-depletion impedes the dynamic dissociation and reassociation between spectrin network nodes and cell membranes³⁸, our finding suggests that the change in cell mechanics is caused by the more persistent spectrin-membrane bindings due to ATP-depletion. Near the critical time window $T_c = 180$ s, ATP-depleted and intact erythrocytes exhibited a remarkable difference in $H(t)$, where even the standard deviations coming from the maximum error propagation obviously separate two data sets each other (clear positive difference in Fig. 6c, $T = 180$ s). The significantly different mechanical responses under these biochemical conditions suggest that intact erythrocytes already undergo the global remodeling of spectrin networks in T_c but ATP-depleted erythrocytes still sustain some spectrin-membrane bindings. Finally, when the cell experiences a longer constriction ($T = 300$ s), the mechanical response of erythrocytes show no clear difference in the recovery time ($\tau \sim 10$ s) in the presence and absence of ATP, implying that extensive spatial constriction ($T = 300$ s) causes the global remodeling of cytoskeletons in both cases (Fig. 6c).

To quantitatively assess our experimental observations, we evaluated the mechanical parameters and time constants according to equation (4). Solid lines in Figs 5a and 6a correspond to the least squared fittings of the experimental data, showing an excellent agreement with the coefficient of determination $R^2 > 0.92$ with an only exception $R^2 = 0.77$ for $T = 60$ s, ATP-depleted erythrocytes. Figure 7 shows the calculated mechanical parameter and time constant as a function of loading times T . Note that the data corresponding to $T = 0$ s (Supplementary Fig. S2) are not included as the response was dominated solely by the elastic jump. Here, the spring constant k_1 was fixed to unity as a reference force unit throughout the fittings, because the force exerted to the cell $f(t)$ by constriction cannot be measured experimentally. The relative significance of each parameter was systematically checked: k_1 and k_2 stay in the same order of magnitude (Supplementary Fig. S3), while c_1 is more than 3 orders of magnitude larger than c_2 . This suggests that both spring constants contribute to determine the elastic properties whereas the viscous property is governed by c_2 . The global plasticity of erythrocytes arising from c_1 is actually quite low, as $H(t)/H(0)$ reaches the saturation level > 0.9 for all the experimental conditions after $t > 10$ s. Thus, we selected c_2/k_1 (Fig. 7a) and $\tau = c_2(k_1 + k_2)/(k_1k_2) = (c_2/k_1)(1 + k_2/k_1)/(k_2/k_1)$ (Fig. 7b) as the representative parameters. The fact that the ratio between c_2/k_1 and τ remained comparable implies that c_2 determines the global shape relaxation kinetics of erythrocytes (Fig. 7c). As presented in Fig. 7a, c_2/k_1 of intact erythrocytes (black) stays low ($c_2/k_1 < 1$) until $T = 120$ s. When the loading time T exceeds $T_c = 180$ s, c_2/k_1 increases to > 1

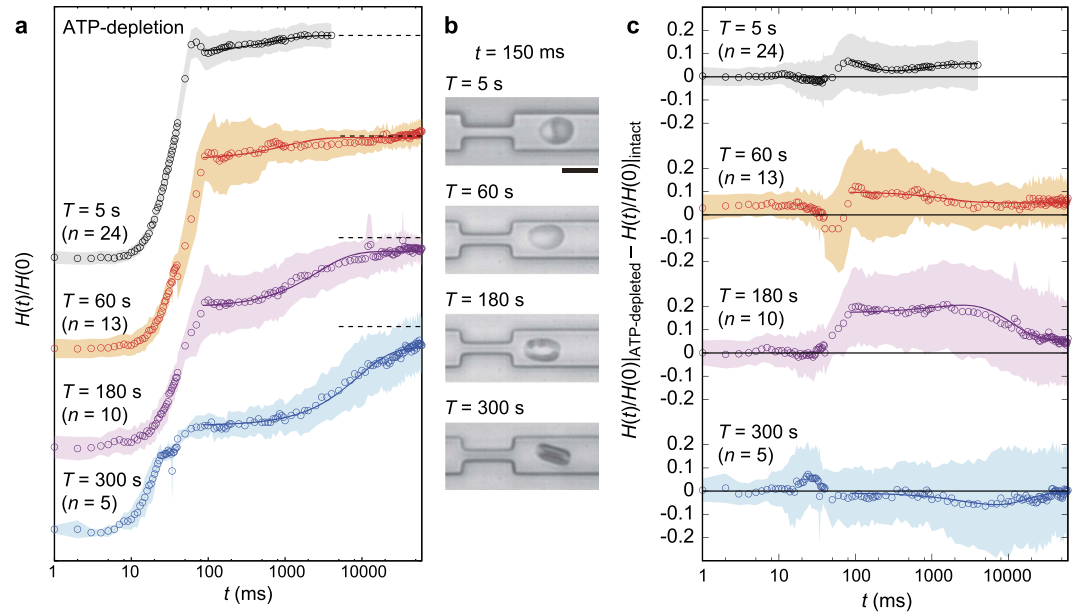


Figure 6. Change in cell height $H(t)$ over time, recorded for ATP-depleted erythrocytes for the different loading times T : 5 s, 60 s, 180 s, and 300 s. (a) Normalized cell height $H(t)/H(0)$. The standard deviations and the fitting curves are represented by shaded areas and solid lines, respectively. Dotted lines represent $H(t)/H(0) = 1$ for each T . Each number of samples n is shown above the graph. (b) Representative snapshot image for each T . Scale bar is $10 \mu\text{m}$. (c) Comparison to intact erythrocytes for each T , where $H(t)/H(0)$ of ATP-depleted erythrocytes exhibited a remarkably faster recovery at $T \sim T_c = 180$ s. S.D. (shaded area) is defined as the maximum error coming from each S.D. of ATP-depleted and intact conditions.

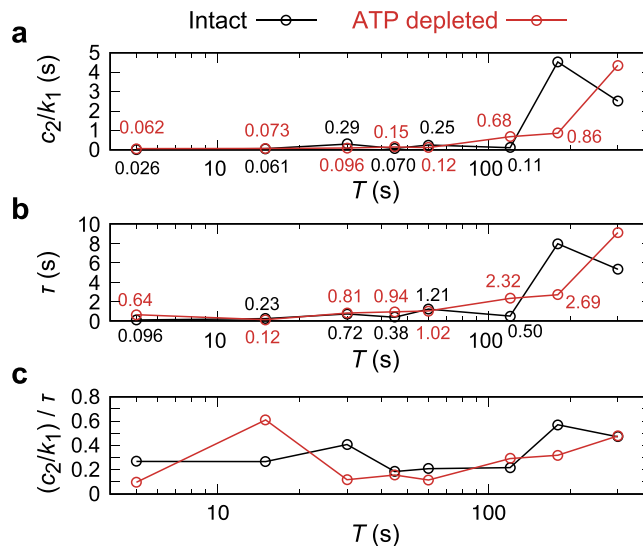


Figure 7. (a) c_2/k_1 , (b) τ , and (c) $(c_2/k_1)/\tau$ for intact (black) and ATP-depleted (red) erythrocytes as a function of loading time T . According to the increasing loading time, c_2/k_1 and τ exhibit a transitional increase at different T . The fact that the ratio $(c_2/k_1)/\tau$ remains almost constant suggests that the global shape recovery is dominated by the internal viscous coefficient c_2 .

and thus the shape recovery becomes slower. In case of ATP-depleted erythrocytes (red), the cells did not exhibit remarkable increase in $c_2/k_1 < 1$ until $T \geq 300$ s. Such a delay in the transition under ATP-depletion was also found for the characteristic recovery time τ (Fig. 7b). In summary, we found that shape recovery occurs rather fast ($\tau_{\text{fast}} = 0.1\text{--}3$ s) at $T \leq 120$ s. After the longer loading time ($T = 180$ s), recovery time τ of intact erythrocytes increases up to $\tau_{\text{slow}} \approx 8$ s, while τ for ATP-depleted erythrocytes remains lower ($\tau < 3$ s). In contrast to the clear changes in c_2/k_1 and τ , neither k_2/k_1 or c_1/k_1 exhibits any systematic dependence on T , irrespective of the presence and absence of ATP (Supplementary Fig. S3).

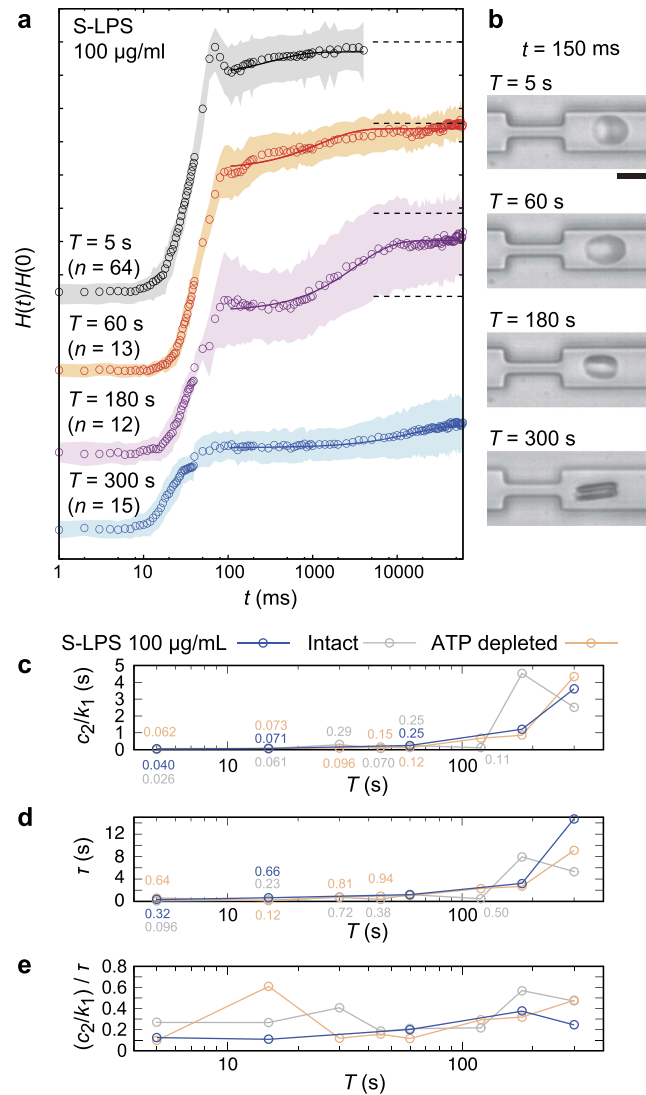


Figure 8. Impact of endotoxin (100 µg/ml S-LPS) on the shape recovery kinetics. (a) Normalized cell heights $H(t)/H(0)$ for the different loading times $T = 5$ s, 60 s, 180 s, and 300 s over time after the exposure to 100 µg/ml S-LPS. The standard deviations and the fitting curves are represented by shaded areas and solid lines, respectively. Dotted lines represent $H(t)/H(0) = 1$ for each T . Each number of samples n is shown above the graph. (b) Representative snapshot image for each T . Scale bar is 10 µm. (c) c_2/k_1 , (d) τ , and (e) $(c_2/k_1)/\tau$ for erythrocytes exposed to 100 µg/ml endotoxin (blue) as a function of T . Results from intact (grey) and ATP-depleted (orange) erythrocytes are plotted for comparison.

Impact of exposure to endotoxin: sepsis model. Finally, we applied our “Catch-Load-Launch” manipulation platform for the potential diagnosis of a blood-related disease: septic shock. Sepsis is a life-threatening disease with systematic inflammatory responses induced by endotoxin (lipopolysaccharide, LPS) molecules released from the outer membranes of Gram-negative bacteria³⁹. Although many reports suggested that the disturbance of smooth microcirculation in sepsis is correlated to the “stiffening” of erythrocytes by LPS^{40,41}, the mechanical diagnosis has been impeded due to the lack of proper design of high throughput methodologies. Here, we examined if our strategy can detect the impact of lipopolysaccharide from *Salmonella minnesota* (S-LPS, see also Supplementary Fig. S4 for molecular detail) on the dynamic mechanical response of human erythrocytes. Figure 8a displays $H(t)/H(0)$ plotted versus t (symbols for the mean values, and shaded areas for the standard deviations) and the corresponding fits (solid lines) for $T = 5$, 60, 180, and 300 s, measured in the presence of 100 µg/ml of S-LPS. The data from other loading times are presented in Supplementary Fig. S5. Figure 8b shows the representative snapshot images at $t = 150$ ms after the launch for each loading time T . Figure 8c–e (blue) shows the representative parameters (c_2/k_1 , τ , and their ratio) plotted versus T , compared to the results from intact (grey) and ATP-depleted (orange) erythrocytes. The mechanical parameters of S-LPS-influenced erythrocytes are very close to those of ATP-depleted erythrocytes, exhibiting similar shift of the critical loading time T_c . On the other hand, k_2/k_1 and c_1/k_1 exhibited no remarkable tendency for all experimental conditions (Supplementary Fig. S6). It should be noted that exposure to S-LPS for only 15 min is sufficient to cause the change in mechanical response,

which is comparable to that of erythrocytes treated for 5 h under ATP-depletion (see Methods), suggesting the significant increase in the cytoskeleton-membrane coupling. This finding is consistent with our previous fluctuation analysis, indicating that LPSs decrease the bending stiffness κ and increase the membrane-cytoskeleton coupling constant γ^{40} . As γ is proportional to the shear modulus dominated by the underlying spectrin network, the increase in cytoskeleton-membrane coupling observed from both passive fluctuation analysis⁴⁰ and active constriction seems to agree well with the previous cone-plate rheometer experiments, suggesting that LPSs make erythrocytes much less deformable.

Discussion

Previously, the fast characteristic recovery time τ_{fast} in the order of 0.1 s was evaluated from the viscoelastic shape recovery after a local deformation by micropipette aspiration^{5,42,43}, the parachute-shaped deformation by multiple optical trapping⁴⁴, and the entire shear deformation by Couette flow⁴⁵. Recent shape fluctuation analyses suggested that the time window of dissociation-reassociation of a spectrin network is about 100 ms on a single node level^{8,29}, whose ATP-dependent, non-equilibrium response could be evidenced by the violation of fluctuation-dissipation theorem^{9,30}. However, although the timescale of fast recovery $\tau_{\text{fast}} = 0.1\text{--}1$ s apparently seems to agree, it is not valid to directly correlate the dissociation-reassociation of a single node and the global shape change. Rather, it seems more plausible to assign τ_{fast} as an intrinsic material constant of erythrocytes, reflecting the surface viscosity and shear modulus⁴². On the other hand, an extremely slow shape recovery with a much longer characteristic time window $\tau_{\text{ex-slow}} \sim 1000$ s was also observed after the extensive diametrical aspiration of a cell for 10–100 min³. Such an extremely slow process was also found in segregated distribution of lipids, cytoskeleton, and mobile transmembrane proteins under micropipette suction ($\tau > 30$ min⁴⁶), existence of “memory” of lateral membrane compositions after applied shear force ($\tau > 4$ h⁴⁷), and spontaneous shape transition between discocytes and echinocytes ($\tau > 10$ h⁴⁸), but there have been no systematic investigations on the mechanism of the extremely slow phenomena.

The experimental strategy proposed in the present work enables to fill the gap between the fast ($\tau_{\text{fast}} = 0.1\text{--}1$ s) and extremely slow ($\tau_{\text{ex-slow}} \sim 1000$ s) shape recovery, unraveling a new time window reflecting the “global” cytoskeletal remodeling. An increasing number of studies suggested that the ATP-dependent deformation of a erythrocyte is originated from the cytoskeletal remodeling by using non-equilibrium contour fluctuation analysis^{8,9,13,29,30,38,40} and shear deformation experiments^{27,28,47}. Therefore, the significant delay of T_c found for ATP-depleted erythrocytes can be attributed to the decrease in the connectivity between spectrin networks and the associated proteins, such as protein 4.1R⁴⁹, band-3^{50,51}, ankyrin⁵², actin⁵³, and spectrin itself⁵⁴. Although exact molecular details are still not clearly identified, our results imply that the slow relaxation (relaxation time: $\tau_{\text{slow}} \sim 10$ s) accompanied by the loading for $T_c \approx 180$ s coincides with the ATP-dependent global remodeling of spectrin cytoskeletons (Fig. 9). This time window is 3 orders of magnitude longer compared to both the fast response ($\tau_{\text{fast}} \sim 0.1$ s) and the local dissociation-reassociation of a single cytoskeletal node (~ 0.1 s), dissecting the global and local dynamics. It should be noted that the measurements of ATP-dependent fluctuation are based on small displacements of the cell rim from its average discocyte shape, which is completely different from the constriction-induced, whole deformation designed in this study that mimics the physiological cell deformation during microcirculation.

In this study, we combined microfluidics and a “robotic pump” system for the mechanical diagnosis of human erythrocytes. By monitoring the dynamic recovery of cell height $H(t)$ upon launching from the narrow path with the aid of a high-speed camera and a visual feedback pressure controller, we could dissect a characteristic loading time T_c for the global cytoskeleton remodeling in the absence and presence of the source of chemical energy (ATP) and endotoxin (S-LPS), which significantly influence the erythrocyte viscoelasticity. Ample evidence suggested a tight correlation between the viscoelastic cell deformation and diseases. For example, sepsis, a systematic inflammatory response syndrome, is caused by the exposure to endotoxin (LPSs), leading to a significant decrease in the deformability. Such a stiffening, characterized by an increase in the shear modulus and thus disturbance of microcirculatory, is much more pronounced for erythrocytes of neonates than those of adults, which makes sepsis more critical for neonates with pre-matured immune systems^{40,41,55}. Another prominent example is the increase in shear modulus of erythrocytes by the progression of malaria infection, demonstrated by micropipette aspiration⁵⁶, optical tweezers⁵⁷, and hydrodynamic shear⁵⁸. As a preliminary attempt to diagnose erythrocytes in a diseased state, we monitored the mechanical response of erythrocytes in the presence of endotoxin S-LPS, mimicking the septic shock. The exposure to 100 $\mu\text{g/ml}$ toxin for 15 min caused a distinct shift in T_c to the longer loading time, which is the same tendency as the mechanical response under ATP-depletion. This finding can be attributed to the inhibited plasticity in membrane-cytoskeleton coupling. Therefore, we concluded that our “Catch-Load-Launch” manipulation platform has a large potential towards the mechanical diagnosis of diseased blood cells.

One of the major problems in mechanical cell diagnosis is the limitation in throughputs. Among several techniques developed in the past years, optical stretcher partly overcame the problem as the technique is non-invasive and can be coupled to a flow chamber^{19,20}. However, optical stretcher has a size limitation of the object diameter (6–30 μm) originating from laser-focus size. Moreover, the applied force cannot be constant during the trapping of a deformable object as the momentum transfer from a laser varies according to the deformation of the object surface. In contrast, our “Catch-Load-Launch” manipulation system is applicable for any object sizes greater than the resolution of microfabrication (~ 1 μm). Moreover, our system specifies the constant deviation amplitude but not the force amplitude, which is physiologically more relevant to the constriction inside microvasculature. The exact deviation control at ultra-high frequency (1000 Hz) and spatial precision ($\Delta x = \pm 0.24$ μm) under the pressure control by the robotic pump enables the actual step-like deformation (Fig. 1b), and thus we can access a wide response time window (1 ms–100 s) in real-space imaging. By utilizing these unique advantages we found that the recovery time τ increases from $\tau_{\text{fast}} \sim 0.1$ s to $\tau_{\text{slow}} \sim 10$ s according to the increase in the loading time

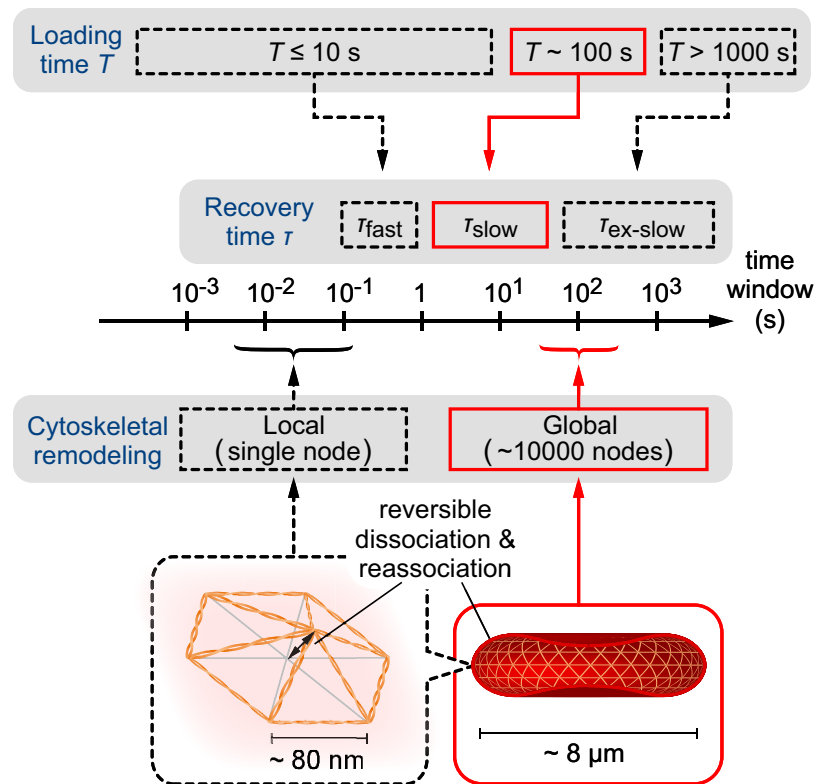


Figure 9. Schematic diagram of characteristic time windows for loading, recovery, and cytoskeletal remodeling. Global cytoskeletal remodeling in 100 s and the corresponding loading T_c result in the slow shape recovery with the characteristic time $\tau_{\text{slow}} \sim 10$ s, as revealed by the present study (denoted by red). The global remodeling of entire spectrin network needs much longer time by 3 orders of magnitude compared to the local remodeling by ATP-dependent reversible dissociation-reassociation of a single node of the triangular lattice.

T from $T = 0$ s to $T = 300$ s through the critical timescale $T_c = 180$ s, which is the characteristic time window for the global remodeling of cytoskeleton. Although the present experiment does not provide the absolute values of these parameters due to the lack of force measurements, the implementation of a force sensor and/or movable wall to apply a specified force in the on-chip robotic pump system could further improve the platform in terms of sensitivity and information content. Last but not least, it should be pointed out that the throughput in our first demonstration (several tens of cells per hour in average) was slightly lower than fully automated optical stretcher equipment (50–100 cells per hour⁵⁹). However, further optimization of the large degree of freedoms of experimental conditions such as cell density, flow speed, programmed procedure, etc., will open up a novel way for the mechanical diagnosis of blood-related diseases based on dynamic response of erythrocytes to spatial constriction.

Methods

Sample preparation. Adult blood was drawn from healthy donors based on the informed consent. All the experiments and experimental protocols for erythrocyte-deformability tests in microchannels were approved by the Ethical Committee of Osaka University and performed following the guideline and regulation. Immediately after the blood drawing, the blood was dispersed at a concentration of 1% (v/v) in standard saline for intact and ATP-depleted conditions, and at the same concentration in saline containing 100 $\mu\text{g}/\text{ml}$ wild-type lipopolysaccharide (S-LPS) for S-LPS influenced condition. ATP-depletion was performed by incubating the above-described 1% blood solution at 37 °C for 5 h. The ATP concentration of the ATP-depleted erythrocyte measured by luciferin-luciferase assay was $43.8 \pm 4.4\%$ of an intact erythrocyte.

Fabrication of microfluidic chips. Microfluidic channel was fabricated in a microfluidic chips made of poly(dimethylsiloxane) (PDMS) resin (SILPOT 184, DOW CORNING TORAY) bounded to a glass substrate. The width of the microchannel, narrow path, and the height of the channel structure were designed as 10 μm , 3 μm , and 3.5 μm , respectively. A master mold for replicating PDMS chips was made by negative photoresist SU8-3005 via standard laser photolithography. PDMS and the curing agent were mixed at a ratio 9:1, and the mixture was degassed under vacuum for 30 min before being poured onto the mold. After the degasification of the PDMS mixture with the mold for another 10 min, the PDMS was baked at 90 °C for 1 h. Afterwards the mold was removed, and two holes for inlet and outlet were punched on the PDMS chip. PDMS surface was treated by plasma cleaner (CUTE 1MP, Femto Science) and bonded on a glass substrate. The inlet and outlet of the fabricated chip were connected to a syringe filled with the above described diluted erythrocyte solution and “robotic

pump” (see Fig. 2 and next paragraph) filled with the standard saline, respectively, via Ethylene tetrafluoroethylene (ETFE) tubes and silicone tubes. Each erythrocyte was deformed and evaluated inside the channel one by one.

Pressure control and observation. Flow of the solution inside the microchannel is basically driven by a constant pressure difference between the inlet and outlet of the channel simply maintained by the atmosphere pressure and gravitational force. The additional pressure control for the temporal cell manipulation was performed by an outlet syringe automatically driven by a connected piezoelectric actuator (PSt 150/5/40 VS10, PIEZOMECHANIK) controlled by a proportional-integral-derivative (PID) algorithm coded in C for processing camera acquisition, cell position detection, voltage input to the piezoelectric actuator through a voltage amplifier (M-2655, MESS TEK), and recording the monitored images, called “robotic pump” in this paper. To capture the exact time window of shape recovery widely ranging from fast elastic response (of the order of ms) and slow viscoelastic relaxation (of the order of min), the input of image was taken at every 1 ms and the output was set at every 1 ms for $0 \text{ ms} \leq t < 40 \text{ ms}$, 10 ms for $40 \text{ ms} \leq t < 200 \text{ ms}$, 50 ms for $200 \text{ ms} \leq t < 1000 \text{ ms}$, 200 ms for $1000 \text{ ms} \leq t < 2000 \text{ ms}$, 500 ms for $2000 \text{ ms} \leq t < 4000 \text{ ms}$, and 1000 ms for $4000 \text{ ms} \leq t \leq 60000 \text{ ms}$ after launch. In the cases of shorter loading times $T = 0 \text{ s}$, 5 s, and 15 s the images were recorded up to 5000 ms, while in the cases of longer loading times $T = 30 \text{ s}$, 45 s, 60 s, 120 s, 180 s, and 300 s, the images were recorded up to 60000 ms.

For the feedback control and observation, the microfluidic chip was mounted on a microscope (IX71, Olympus) with a $\times 40$ objective lens (N.A. = 0.6) connected to a high-speed camera (IDP-Express R2000, Photron). The resultant pixel size of image acquisition was $0.24 \mu\text{m}$, which is the spatial precision itself of the manipulation. The camera view was set around the narrow path of the microchannel, and the recording frequency was set at 1000 Hz, which makes it possible to manipulate the cell position in the rapid flow in the thin microchannel by the visual feedback pressure controller. Using this system we performed the three-step Catch-Load-Launch manipulation (see main text).

Data analysis. Obtained sequential images were processed in a custom routine developed in MATLAB R2015a with Image processing toolbox (MathWorks). Using the image in the catching phase, data screening was conducted for the cell with high ellipsoidal eccentricity (> 0.5) to avoid the analyses of unexpected asymmetric deformation inside the narrow path. Then the cell shape and height in the launching phase was measured based on the binarized images calculated from the original bright field images. The changes in cell orientation after launch was corrected in every image before the height calculation based on the angular degree of the ellipsoidal minor axis of the binarized cell. Least square fittings of the cell height changes for various loading time $T = 0 \text{ s}$, 5 s, 15 s, 30 s, 45 s, 60 s, 120 s, 180 s, and 300 s with equation (4) was performed using the mean cell height data after 80 ms (standard saline and that with ATP-depletion assay) and for $T = 0 \text{ s}$, 5 s, 15 s, 60 s, 180 s, and 300 s after 100 ms (standard saline dissolving $100 \mu\text{g/ml}$ S-LPS) when the cells stopped initial elastic responses and entered the viscoelastic regime in the launching phase.

More details of SLE model. We derived analytical solution of standard linear elastic (SLE) model in the launching phase in Catch-Load-Launch experiment. The deformation length $y(t)$ becomes a single exponential function with a constant offset A_1 and a constant coefficient A_2 :

$$y(t) = A_1 + A_2 e^{-\frac{t-T}{\tau}}, \quad (T \leq t). \quad (5)$$

With the mechanical parameters k_1 , k_2 , c_1 , and c_2 , these constants A_1 and A_2 are expressed as

$$A_1 \equiv \tau \dot{y}(T) + y(T), \quad (6)$$

$$A_2 \equiv -\tau \dot{y}(T) e^{\frac{T}{\tau}}, \quad (7)$$

where

$$y(T) = y_c - \frac{k_1 y_1(T) + k_2 y_2(T)}{k_1 + k_2}, \quad (T \leq t), \quad (8)$$

$$\dot{y}(T) = \frac{1}{c_1 \tau} \left\{ \frac{C_+}{\rho_+} (e^{\rho_+ T} - 1) + \frac{C_-}{\rho_-} (e^{\rho_- T} - 1) \right\} - \frac{y(T)}{\tau}, \quad (T \leq t), \quad (9)$$

$$y_1(t) = \frac{C_+}{(k_1 + k_2)(\rho_+ + \tau^{-1})} \left(\rho_+ e^{\rho_+ t} + \tau^{-1} e^{-\frac{t}{\tau}} \right) + \frac{C_+}{k_1 \tau (\rho_+ + \tau^{-1})} \left(e^{\rho_+ t} + e^{-\frac{t}{\tau}} \right) \\ + \frac{C_-}{(k_1 + k_2)(\rho_- + \tau^{-1})} \left(\rho_- e^{\rho_- t} + \tau^{-1} e^{-\frac{t}{\tau}} \right) + \frac{C_-}{k_1 \tau (\rho_- + \tau^{-1})} \left(e^{\rho_- t} + e^{-\frac{t}{\tau}} \right), \quad (10)$$

$$y_2(t) = \frac{C_+}{(k_1 + k_2)(\rho_+ + \tau^{-1})} \left(\rho_+ e^{\rho_+ t} + \tau^{-1} e^{-\frac{t}{\tau}} \right) + \frac{C_-}{(k_1 + k_2)(\rho_- + \tau^{-1})} \left(\rho_- e^{\rho_- t} + \tau^{-1} e^{-\frac{t}{\tau}} \right), \quad (11)$$

$$\rho_{\pm} \equiv \frac{1}{2} \left[- \left(\frac{k_2}{c_2} + \frac{k_1 + k_2}{c_1} \right) \pm \sqrt{\left(\frac{k_2}{c_2} - \frac{k_1 - k_2}{c_1} \right)^2 + \frac{4k_1 k_2}{c_1^2}} \right], \quad (12)$$

$$C_{\pm} \equiv \pm \frac{(k_1 + k_2)\rho_{\pm} + \frac{k_1 k_2}{c_2}}{\rho_{\pm} - \rho_{\mp}} y_c. \quad (13)$$

Here y_c is the deformation length by the constraint in the narrow path of the channel with $H_c = 3 \mu\text{m}$ in width, namely, $y_c = H(0) - H_c$. In the analyses in this study, we fixed a parameter k_1 as unity for each loading time condition, and evaluated the ratios between other parameters k_2/k_1 , c_1/k_1 , and c_2/k_1 . The validation of this assumption is discussed with the results in main text.

References

- Evans, E. A. & La Celle, P. L. Intrinsic material properties of the erythrocyte membrane indicated by mechanical analysis of deformation. *Blood* **45**, 29–43 (1975).
- Evans, E. A., Waugh, R. & Melnik, L. Elastic area compressibility modulus of red cell membrane. *Biophys. J.* **16**, 585–595 (1976).
- Markle, D. R., Evans, E. A. & Hochmuth, R. M. Force relaxation and permanent deformation of erythrocyte membrane. *Biophys. J.* **42**, 91–98 (1983).
- Discher, D. E. & Mohandas, N. Kinematics of red cell aspiration by fluorescence-imaged microdeformation. *Biophys. J.* **71**, 1680–1694 (1996).
- Bronkhorst, P. J. H. *et al.* A new method to study shape recovery of red blood cells using multiple optical trapping. *Biophys. J.* **69**, 1666–1673 (1995).
- Lenormand, G., Hénon, S., Richert, A., Siméon, J. & Gallet, F. Direct measurement of the area expansion and shear moduli of the human red blood cell membrane skeleton. *Biophys. J.* **81**, 43–56 (2001).
- Lim, C. T., Dao, M., Suresh, S., Sow, C. H. & Chew, K. T. Large deformation of living cells using laser traps. *Acta Mater.* **52**, 1837–1845 (2004).
- Betz, T., Lenz, M., Joanny, J.-F. & Sykes, C. ATP-dependent mechanics of red blood cells. *Proc. Nat. Acad. Sci. USA* **106**, 15320–15325 (2009).
- Turlier, H. *et al.* Equilibrium physics breakdown reveals the active nature of red blood cell membrane fluctuations. *Nat. Phys.* **12**, 513–519 (2016).
- Brochard, F. & Lennon, J. F. Frequency spectrum of the flicker phenomenon in erythrocytes. *J. Phys. France* **36**, 1035–1047 (1975).
- Strey, H., Peterson, M. & Sackmann, E. Measurement of erythrocyte membrane elasticity by flicker eigenmode decomposition. *Biophys. J.* **69**, 476–488 (1995).
- Gov, N., Zilman, A. G. & Safran, S. Cytoskeleton confinement and tension of red blood cell membranes. *Phys. Rev. Lett.* **90**, 228101 (2003).
- Yoon, Y.-Z. *et al.* Flickering analysis of erythrocyte mechanical properties: dependence on oxygenation level, cell shape, and hydration level. *Biophys. J.* **97**, 1606–1615 (2009).
- Schmid-Schönbein, H., Gosen, J. V., Heinich, L., Klose, H. J. & Volger, E. A counter-rotating "rheoscope chamber" for the study of the microrheology of blood cell aggregation by microscopic observation and microphotometry. *Microvas. Res.* **6**, 366–376 (1973).
- Fischer, T. M., Stöhr-liesen, M. & Schmid-Schönbein, H. The red cell as a fluid droplet: Tank tread-like motion of the human erythrocyte membrane in shear flow. *Science* **202**, 894–896 (1978).
- Quinn, D. J. *et al.* Combined simulation and experimental study of large deformation of red blood cells in microfluidic systems. *Ann. Biomed. Eng.* **39**, 1041–1050 (2011).
- Zheng, Y., Shojaei-Baghini, E., Azad, A., Wang, C. & Sun, Y. High-throughput biophysical measurement of human red blood cells. *Lab Chip* **12**, 2560–2567 (2012).
- Wan, J., Ristenpart, W. D. & Stone, H. A. Dynamics of shear-induced ATP release from red blood cells. *Proc. Nat. Acad. Sci. USA* **105**, 16432–16437 (2008).
- Guck, J., Ananthakrishnan, R., Moon, T. J., Cunningham, C. C. & Käs, J. Optical deformability of soft biological dielectrics. *Phys. Rev. Lett.* **84**, 5451–5454 (2000).
- Guck, J. *et al.* Optical deformability as an inherent cell marker for testing malignant transformation and metastatic competence. *Biophys. J.* **88**, 3689–3698 (2005).
- Gossett, D. R. *et al.* Hydrodynamic stretching of single cells for large population mechanical phenotyping. *Proc. Nat. Acad. Sci. USA* **109**, 7630–7635 (2012).
- Otto, O. *et al.* Real-time deformability cytometry: on-the-fly cell mechanical phenotyping. *Nat. Methods* **12**, 199–202 (2015).
- Guck, J. & Chilvers, E. R. Mechanics meets medicine. *Sci. Transl. Med.* **5**, 212fs41 (2013).
- Wyss, H. M. Cell mechanics: Combining speed with precision. *Biophys. J.* **109**, 1997–1998 (2015).
- Tan, Y., Sun, D. & Huang, W. Mechanical modeling of red blood cells during optical stretching. *J. Biochem. Eng.* **132**, 044504 (2010).
- Mietke, A. *et al.* Extracting cell stiffness from real-time deformability cytometry: Theory and experiment. *Biophys. J.* **109**, 2023–2036 (2015).
- An, X., Lecomte, M. C., Chasis, J. A., Mohandas, N. & Gratzel, W. Shear-response of the spectrin dimer-tetramer equilibrium in the red blood cell membrane. *J. Biol. Chem.* **277**, 31796–31800 (2002).
- Li, J., Lykotrafitis, G., Dao, M. & Suresh, S. Cytoskeletal dynamics of human erythrocyte. *Proc. Nat. Acad. Sci. USA* **104**, 4937–4942 (2007).
- Rodríguez-García, R. *et al.* Direct cytoskeleton forces cause membrane softening in red blood cells. *Biophys. J.* **108**, 2794–2806 (2015).
- Wojdyła, M., Raj, S. & Petrov, D. Nonequilibrium fluctuations of mechanically stretched single red blood cells detected by optical tweezers. *Eur. Biophys. J.* **42**, 539–547 (2013).

31. Sakuma, S. *et al.* Red blood cell fatigue evaluation based on the close-encountering point between extensibility and recoverability. *Lab Chip* **14**, 1135–1141 (2014).
32. Murakami, R. *et al.* Catch, load and launch toward on-chip active cell evaluation. Proc. IEEE International Conference on Robotics and Automation (ICRA 2016), Stockholm (2016).
33. Pivkin, I. V. *et al.* Biomechanics of red blood cells in human spleen and consequences for physiology and disease. *Proc. Nat. Acad. Sci. USA* **113**, 7804–7809 (2016).
34. Bausch, A. R., Ziemann, F., Boulbitch, A. A., Jacobson, K. & Sackmann, E. Local measurements of viscoelastic parameters of adherent cell surfaces by magnetic bead microrheometry. *Biophys. J.* **75**, 2038–2049 (1998).
35. Skalak, R. & Branemark, P.-I. Deformation of red blood cells in capillaries. *Science* **164**, 717–719 (1969).
36. Noguchi, H. & Gompfer, G. Shape transitions of fluid vesicles and red blood cells in capillary flows. *Proc. Nat. Acad. Sci. USA* **102**, 14159–14164 (2005).
37. Braunnmüller, S., Schmid, L., Sackmann, E. & Franke, T. Hydrodynamic deformation reveals two coupled modes/time scales of red blood cell relaxation. *Soft Matter* **8**, 11240–11248 (2012).
38. Gov, N. S. & Safran, S. A. Red blood cell membrane fluctuations and shape controlled by ATP-induced cytoskeletal defects. *Biophys. J.* **88**, 1859–1874 (2005).
39. Lüdertitz, O. *et al.* *Current Topics in Membranes and Transport* (Academic Press: New York, 1982).
40. Ito, H. *et al.* Quantification of the influence of endotoxins on the mechanics of adult and neonatal red blood cells. *J. Phys. Chem. B* **119**, 7837–7845 (2015).
41. Pöschl, J. M. B. & Linderkamp, O. Effect of lipid A on the deformability, membrane rigidity, and geometry of human adult red blood cells. *Eur. J. Clin. Invest.* **22**, 625–629 (1992).
42. Evans, E. A. & Hochmuth, R. M. Membrane viscoelasticity. *Biophys. J.* **16**, 1–11 (1976a).
43. Waugh, R. & Evans, E. A. Viscoelastic properties of erythrocyte membranes of different vertebrate animals. *Microvas. Res.* **12**, 291–304 (1976).
44. Hochmuth, R. M., Worthy, P. R. & Evans, E. A. Red Cell Extensional Recovery and the Determination of Membrane Viscosity. *Biophys. J.* **26**, 101–114 (1979).
45. Baskurt, O. K. & Meiselman, H. J. Determination of red blood cell shape recovery time constant in a couette system by the analysis of light reflectance and ektacytometry. *Biorheology* **33**, 489–503 (1996).
46. Discher, D. E., Mohandas, N. & Evans, E. A. Molecular maps of red cell deformation: Hidden elasticity and *in situ* connectivity. *Science* **266**, 1032–1035 (1994).
47. Fischer, T. M. Shape memory of human red blood cells. *Biophys. J.* **86**, 3304–3313 (2004).
48. Fischer, T. M. Creep and stress relaxation of human red cell membrane. *Biomech. Model Mechanobiol.* doi: 10.1007/s10237-016-0813-2 (2016).
49. Manno, S., Takakuwa, Y. & Mohandas, N. Modulation of erythrocyte membrane mechanical function by protein 4.1 phosphorylation. *J. Biol. Chem.* **280**, 7581–7587 (2005).
50. Harrison, M. L., Rathinavelu, P., Arese, P., Geahlen, R. L. & Low, P. S. Role of band 3 tyrosine phosphorylation in the regulation of erythrocyte glycolysis. *J. Biol. Chem.* **266**, 4106–4111 (1991).
51. Ferru, E. *et al.* Regulation of membrane-cytoskeletal interactions by tyrosine phosphorylation of erythrocyte band 3. *Blood* **117**, 5998–6006 (2011).
52. Lu, P.-W., Soong, C.-J. & Tao, M. Phosphorylation of ankyrin decreases its affinity for spectrin tetramer. *J. Biol. Chem.* **260**, 14958–14964 (1985).
53. Tuvia, S., Levin, S., Bitler, A. & Korenstein, R. Mechanical fluctuations of the membrane-skeleton are dependent on F-actin ATPase in human erythrocytes. *J. Cell Biol.* **141**, 1551–1561 (1998).
54. Manno, S., Takakuwa, Y., Nagao, K. & Mohandas, N. Modulation of erythrocyte membrane mechanical function by β -spectrin phosphorylation and dephosphorylation. *J. Biol. Chem.* **270**, 5659–5665 (1995).
55. Pöschl, J. M. B., Leray, C., Ruef, P., Cazenave, J. P. & Linderkamp, O. Endotoxin binding to erythrocyte membrane and erythrocyte deformability in human sepsis and *in vitro*. *Crit. Care Med.* **31**, 924–928 (2003).
56. Gleinster, F. K., Coppel, R. L., Cowman, A. F., Mohandas, N. & Cooke, B. M. Contribution of parasite proteins to altered mechanical properties of malaria-infected red blood cells. *Blood* **99**, 1060–1063 (2002).
57. Suresh, S. *et al.* Connections between single-cell biomechanics and human disease states: gastrointestinal cancer and malaria. *Acta Biomater.* **1**, 15–30 (2005).
58. Suwanarusk, R. *et al.* The deformability of red blood cells parasitized by *Plasmodium falciparum* and *P. vivax*. *J. Infect. Dis.* **189**, 190–194 (2004).
59. Lincoln, B. *et al.* Reconfigurable microfluidic integration of a dual-beam laser trap with biomedical applications. *Biomed. Microdevices* **9**, 703–710 (2007).

Acknowledgements

We thank Y. Sakata for providing blood samples as a research cooperation, and N. Kuss for helpful comments on the blood-related diseases. H.I. thanks JSPS (JP16H06933), Grants-in-Aid for JSPS Research Fellowship for Young Scientists (JP13J01297) and Sasakawa Scientific Research Grant from The Japan Science Society (28–233). C.-H.D.T. thanks JSPS (JP16K18051) for support. M.K. thanks JSPS (JP15H05761) for support. M.T. thanks JSPS (JP26247070), EUFP7 “SoftActive”, and German Science Foundation (CRC1129P3) for support.

Author Contributions

H.I., M.K. and M.T. designed the project; H.I., R.M., S.S., M.K., and M.T. designed the experimental setup and procedure; H.I., R.M., and S.S. performed the experiments; T.G. and K.B. prepared lipopolysaccharide samples; H.I. analyzed the data; All authors discussed and wrote the manuscript.

Additional Information

Supplementary information accompanies this paper at <http://www.nature.com/srep>

Competing financial interests: The authors declare no competing financial interests.

How to cite this article: Ito, H. *et al.* Mechanical diagnosis of human erythrocytes by ultra-high speed manipulation unraveled critical time window for global cytoskeletal remodeling. *Sci. Rep.* **7**, 43134; doi: 10.1038/srep43134 (2017).

Publisher's note: Springer Nature remains neutral with regard to jurisdictional claims in published maps and institutional affiliations.



This work is licensed under a Creative Commons Attribution 4.0 International License. The images or other third party material in this article are included in the article's Creative Commons license, unless indicated otherwise in the credit line; if the material is not included under the Creative Commons license, users will need to obtain permission from the license holder to reproduce the material. To view a copy of this license, visit <http://creativecommons.org/licenses/by/4.0/>

© The Author(s) 2017